Superconductor
Science and
Technology

PAPER • **OPEN ACCESS**

Evidence of multiscale supercurrents in K-doped $BaFe_2As_2$

To cite this article: Chiara Tarantini *et al* 2025 *Supercond. Sci. Technol.* **38** 045023

OPEN ACCESS
IOP Publishing
Superconductor Science and Technology
Supercond. Sci. Technol. **38** (2025) 045023 (11pp)
https://doi.org/10.1088/1361-6668/adc633

Evidence of multiscale supercurrents in K-doped $BaFe_2As_2$

Chiara Tarantini[1,*], Shah Alam Limon[1], Keyou Mao[1], Eric E Hellstrom[1,2,3] and Fumitake Kametani[1,2]

[1] National High Magnetic Field Laboratory, Florida State University, Tallahassee, FL 32310, United States of America
[2] Department of Mechanical Engineering, FAMU-FSU College of Engineering, Florida State University, Tallahassee, FL 32310, United States of America
[3] Department of Materials Science and Engineering, FAMU-FSU College of Engineering, Florida State University, Tallahassee, FL 32310, United States of America

E-mail: tarantini@asc.magnet.fsu.edu

Received 10 February 2025, revised 14 March 2025
Accepted for publication 26 March 2025
Published 8 April 2025

Abstract

K-doped $BaAs_2Fe_2$ (K-Ba122) superconductor is a promising material for applications. However, it has been found challenging to achieve high critical current density (J_c) in untextured bulk sample. In this paper we investigated bulk samples prepared by varying the milling energy density, which affects the grain and grain boundary microstructures, and we investigated their magnetic performance to better understand what causes their different J_c. We found that in our samples, which all have small grain size, T_c does not appear directly correlated to J_c. Moreover, AC susceptibility reveals in at least one case obvious signs of multiscale supercurrents, not caused by granularity but that directly influence the overall J_c performance. Considering the microstructural features and the magnetization response we ascribed the J_c differences to lack of connectivity on a larger scale due to nano-cracks at some grain boundaries, which subdivided the samples into macroscopic regions and inevitably limited the overall performance. We discuss possible routes to overcome those extrinsic current-blocking defects.

Keywords: Fe-based superconductors, K-doped $BaAs_2Fe_2$, critical current density, AC susceptibility, transmission electron microscopy

1. Introduction

Fe-based superconductors (FBSs) were first discovered in 2006 [1, 2] and soon after several different compounds and families were found [3–6] reaching a maximum critical temperature, T_c, at ambient pressure of 55 K [7]. FBSs are of interest for applications not only because of their moderately high T_c, but also due to their high upper critical field, H_{c2} [8–11], which enable applications in high-field, such as fusion and accelerator magnets. Within the FBSs, the family that attracts most of the attention from an application prospective is the '122' phase with $AEFe_2As_2$ as the parent compound (*AE* being an alkaline-earth metal like Ba or Sr). Superconductivity can be induced by several chemical substitutions, like Co on the Fe site [12], K on the *AE* site [3] or the isovalent P substitution on the As site [13]. The $Ba_{1-x}K_xFe_2As_2$ phase (K-Ba122) is of particular interest because it has the highest T_c in the 122 family and, despite the lower T_c with respect to the '1111' *RE*FeAsO-type (*RE* being a rare-earth element) family, all 122 compounds have low anisotropy [9, 10, 14, 15], a highly desirable attribute to avoid incurring intrinsic grain boundary (GB) limitations. A recent bicrystal study demonstrated that K-Ba122 has better GB transparency than cuprates [16], making high critical current density potentially achievable also in polycrystalline samples. The implications are that wires

* Author to whom any correspondence should be addressed.

and tapes can be realized by the simple powder-in-tube (PIT) method [17–22]. Although FBS coated conductors have also been realized reaching high J_c thanks to the biaxial texturing [23–27], their shape factor and fabrication cost are drawbacks, making PIT a better performance/cost compromise. For the realization of magnets, untextured K-Ba122 round wires are in general preferable to tapes, but the partially textured tapes typically have higher J_c [17]. These values are however still far from J_c obtained in single crystals [28–30] or the remarkably high J_c of films [31, 32], where the cause of the ameliorated J_c performance was identified in pinning effects induced by low-angle grain boundaries.

To understand what limits the properties in polycrystalline materials, several studies investigated whether the GBs are intrinsically blocking current. Our works have been focused on the bulk samples because it is preferable for the investigation of GB transparency in randomly oriented samples. Moreover, the processing can be similar to the preparation of powders for wires and tapes, typically mixing of the components by using ball-milling followed by a sintering heat treatment (HT). It was previously observed that secondary phases can still be present at GBs forming extrinsic current blockers [33, 34], which however can be eliminated by improving the material processing. Despite the improvement made by removing those secondary phases [35, 36], the J_c performance in bulk samples is not yet as high as in tapes, which have the advantages of partial texturing. The previously mentioned bicrystal study, which reported a J_c(12 K, 1 T) across a 24° misorientation GB exceeding 0.1 MA cm^{-2} [16], does not explain the underwhelming performance of bulks. To address this, here we investigated the microstructural and electromagnetic properties of K-Ba122 bulk samples. It was previously demonstrated by Tokuta *et al* [37] that the microstructure and superconductivity properties of Co-doped Ba-122 can be significantly modified by changing the milling energy density. Here we followed a similar approach by changing the milling energy density for the first HT of our K-Ba122 samples. Specifically, we used AC susceptibility, which is very effective in granular samples for separating between the intra-grain and INTER-grain contributions. The former arises from current within individual grains, while the latter is determined by current crossing the GBs. In fact, AC susceptibility has been employed to investigate granularity in both polycrystalline HTS samples [38–42] and polycrystalline FBSs, like for instance in the '11' ($FeSe_{1-x}Te_x$) and 1111 phases [43–45], as this technique reveals double χ_1' transitions and two χ_1'' peaks corresponding to the intra- and INTER-grain contributions. The intra-grain contribution is associated with the highest temperature features and the intra-grain χ_1'' peak is always smaller than the INTER-grain peak [46]. This is an important detail to keep in mind for the correct interpretation of the results presented here for our K-Ba122 samples. In fact, our results lead to a quite different scenario compared with typical granular behavior.

2. Experimental

The K-doped Ba122 polycrystalline samples were made with a nominal composition of $Ba_{0.6}K_{0.4}Fe_2As_2$. The high purity precursors are mixed in the stoichiometric ratio (purities: 99.99% crystalline dendritic solid Ba pieces, 99.95% K paste, ⩾99.99% Fe powders and ⩾99.99999% As powders) in a high-performance glovebox (O_2 level ⩽ 0.005 ppm and H_2O level ⩽0.06 ppm). We employed 2 ball millings and 2 HTs procedure for the sample preparation and synthesis [35]. The three samples differ in their first milling energy density (E_{BM}) that was varied between 65, 100 and 200 MJ kg^{-1}, calculated as in [37, 47]. The mixed powders were then welded in Nb/steel crucibles, densified in a cold isostatic press, and received a first HT at 750 °C for 10 h in ambient pressure. 750 °C was chosen because it was previously found to produce the best samples [35, 48]. The three heat-treated samples were then ball milled (E_{BM} = 40 MJ kg^{-1}), the powders were resealed in a crucible and received a second HT at 600 °C/10 h at 193 MPa in the hot isostatic press (HIP). The second milling and HT were identical for the three samples. After the second HT, Rietveld analysis confirmed a nearly optimal doping with 38%–39% of K. These samples were selected from a wider systematic study because of their interesting properties [49]. Below we refer to these samples by their first milling energy density and by their high-field J_c ranking as summarized in table 1 (e.g. 65-Medium-J_c is the sample prepared at 65 MJ kg^{-1} and has the intermediate high-field J_c).

The fully heat-treated samples were extracted from the crucible, cut into bars and polished into a well-defined parallelepipedal shape for magnetic characterizations. Hysteresis loops were performed in a 14 T Oxford Vibrating Sample Magnetometer and the magnetic J_c(4.2 K) was estimated by the Bean critical state model. AC susceptibility was performed in a Quantum Design 9 T-PPMS applying AC field, H_{ac}, with amplitude variation from 0.01 mT to 1.5 mT and frequency from 13 to 757 Hz (most characterizations were performed at 73 Hz). The background DC field, H_{DC}, was increased up to 9 T. The first harmonic χ_1 was properly calculated using the sample size and demagnetization factor [39, 50].

A JEOL ARM200cF was used to perform bright field transmission electron microscopy (BF TEM) and high-angle annular dark-field scanning TEM (HAADF STEM) imaging as well as chemical analysis by energy dispersive x-ray spectroscopy (EDS). The samples for TEM/STEM were prepared by focused ion beam in a Thermo Fisher FEI Helios G4 UC scanning electron microscope.

3. Results

3.1. Magnetization J_c

Figure 1 shows the J_c(H) curves for the three samples. We found that the sample prepared with a milling energy of 100 MJ kg^{-1} has the largest J_c over the entire field range with a self-field J_c of about 2×10^5 A cm^{-2} and reaching a J_c(10 T) of about 1.4×10^4 A cm^{-2}. The 65 MJ kg^{-1} sample is the second best across most of the field range but exhibits a double cross-over with the 200 MJ kg^{-1} sample at 0.5–1 T shown in the inset of figure 1. Its J_c shows a sharp decline for applied field up to 1 T, followed by a rather weak field dependence at higher fields. J_c of the 200 MJ kg^{-1} sample is inferior in both low and high fields. Based on their J_c performance at high-field, these samples will be referred as '100-Higher-J_c'

Table 1. Sample names, milling energy density E_{BM} for the first milling, critical current density J_c at 4.2 K and different magnetic field for the three fully heat-treated K-doped Ba122 samples.

Sample name	E_{BM} MJ kg^{-1}	J_c(0.25 T,4.2 K) A cm^{-2}	J_c(0.5 T,4.2 K) A cm^{-2}	J_c(1 T,4.2 K) A cm^{-2}	J_c(10 T,4.2 K) A cm^{-2}
65-Medium-J_c	65	6.59×10^4	3.73×10^4	2.36×10^4	7.3×10^3
100-Higher-J_c	100	1.94×10^5	1.39×10^5	7.93×10^4	1.38×10^4
200-Lower-J_c	200	5.33×10^4	3.84×10^4	2.35×10^4	3.1×10^3

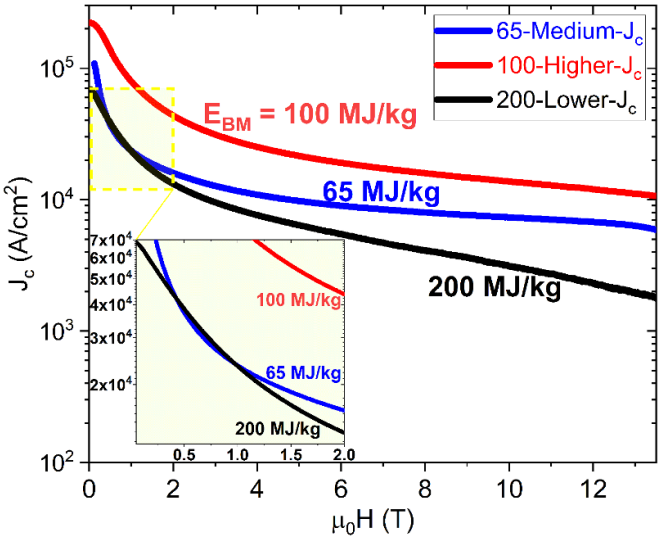

Figure 1. Field dependence of J_c(4.2 K) for three K-Ba122 samples prepared varying the first milling energy density (E_{BM}). J_c is estimated from hysteresis loops using the Bean model. In the inset a magnification showing the double crossover of the curves for the 65 and 200 MJ kg^{-1} samples.

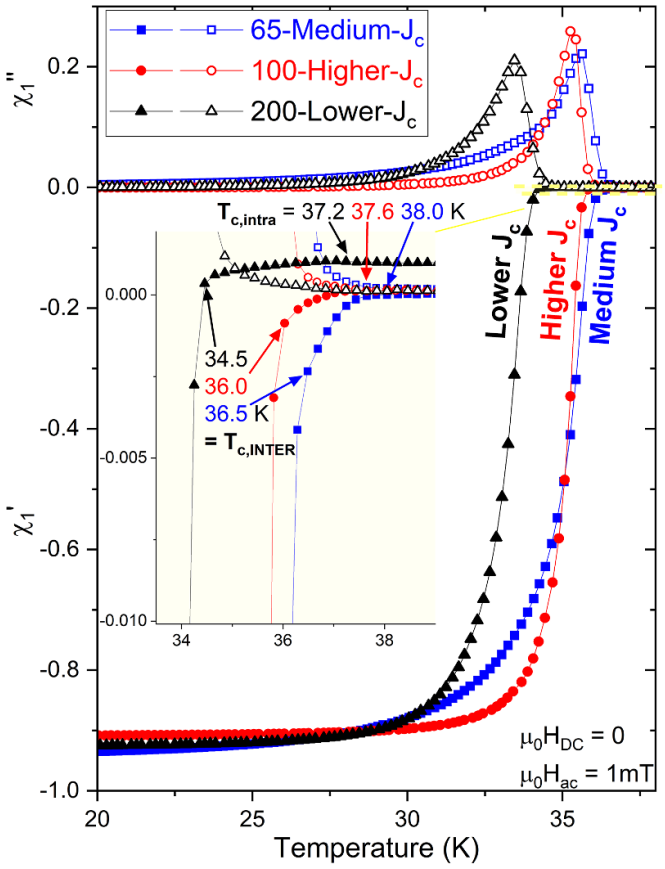

Figure 2. AC susceptibility measured at zero DC field and $\mu_0 H_{ac} = 1$ mT ($f = 211$ Hz) for the three K-Ba122 samples. In the inset a magnification of the region near the transition onset.

for the 100 MJ kg^{-1}, '65-Medium-J_c' for the 65 MJ kg^{-1}, '200-Lower-J_c' for the 200 MJ kg^{-1}. Table 1 summarizes the sample names, the main synthesis differences and their in-field J_c performance.

3.2. AC susceptibility and irreversibility lines

Figure 2 reports an example of the AC susceptibility measured at $\mu_0 H_{ac} = 1$ mT and zero DC field for the three samples. At first glance we can observe sharp diamagnetic transitions in χ_1' for both the 200-Lower-J_c and 100-Higher-J_c samples but the former clearly has a much lower T_c than the other two samples. The 65-Medium-J_c sample appears to have the highest onset but with a much broader transition. The dissipative χ_1'' peaks reveal clear differences in their shapes. 100-Higher-J_c shows the sharpest peak, followed by the 200-Lower-J_c, whose peak however is at much lower temperature, and then 65-Medium-J_c, which reveals a clear long, extended low-temperature tail. As highlighted in the figure 2 inset, a closer inspection near the onset of χ_1' reveals that the T_c onset is actually noticeably higher in temperature than the onsets of the sharp diamagnetic drops, although it produces a very small signal. We interpreted the first deviation from the normal state as the T_c onset of the highest temperature grains, attributed to intra-grain shielding (denoted as $T_{c,\mathrm{intra}}$). In contrast, the onset of the sharp diamagnetic drops is associated with the onset of bulk superconductivity, derived from inter-grain shielding current ($T_{c,\mathrm{INTER}}$). The $T_{c,\mathrm{intra}}$ values are relatively similar in the samples, varying from a maximum of 38.0 K in 65-Medium-J_c, to 37.6 K in 100-Higher-J_c, and 37.2 K in 200-Lower-J_c. It should be pointed out that such a high T_c onset (corresponding to $T_{c,\mathrm{intra}}$) is never detected by DC magnetization in our samples after the second milling and HT (although it is detected after the first HT). The difficulty in detecting the intra-grain T_c is presumably caused by the small grain size, significantly smaller than the penetration depth ($\lambda_{ab} \sim$ 200–250 nm) [48]. The second onsets, $T_{c,\mathrm{INTER}}$, are at 36.5 K and 36.0 K for the 65-Medium and 100-Higher-J_c samples, respectively. $T_{c,\mathrm{INTER}}$ of the 200-Lower-J_c sample is obviously suppressed to 34.5 K. Table 2 summarizes these results as well as the difference between the INTER- and intra-grain T_c.

Table 2. INTER- and intra-grain T_c and their separation for the three K-doped Ba122 samples. The $T_{c,intra}$ and $T_{c,INTER}$ are evaluated as explained in the text.

Sample name	$T_{c,INTER}$ K	$T_{c,intra}$ K	$T_{c,intra}$ -$T_{c,INTER}$ K
65-Medium-J_c	36.5	38.0	1.5
100-Higher-J_c	36	37.6	1.6
200-Lower-J_c	34.5	37.2	2.7

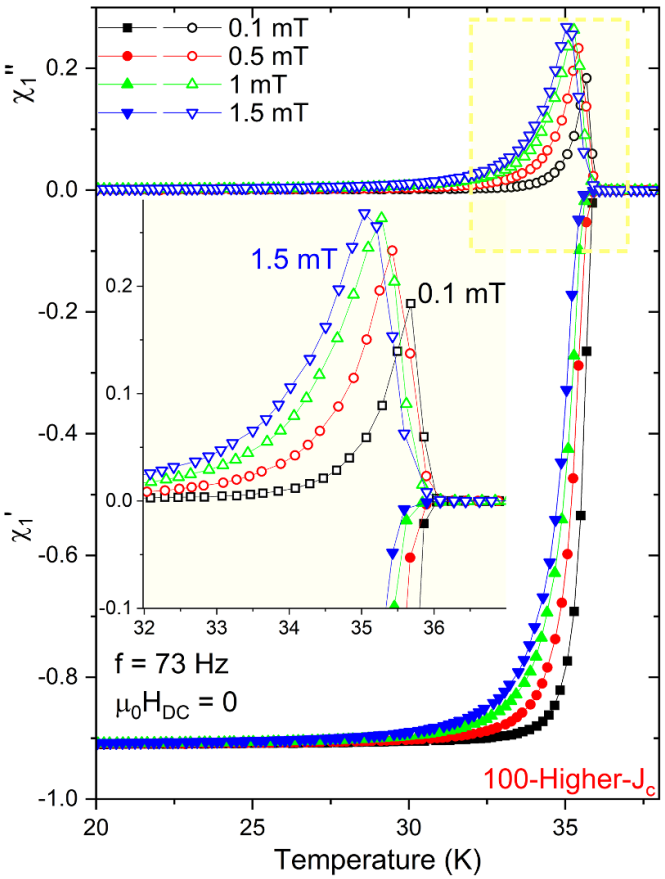

Figure 3. AC susceptibility for the 100-Higher-J_c K-Ba122 sample measured with zero DC field and $\mu_0 H_{ac}$ from 0.1 to 1.5 mT ($f = 73$ Hz). In the inset a magnification of the χ_1'' peaks shows the sharpening of the peaks with decreasing H_{ac} amplitude.

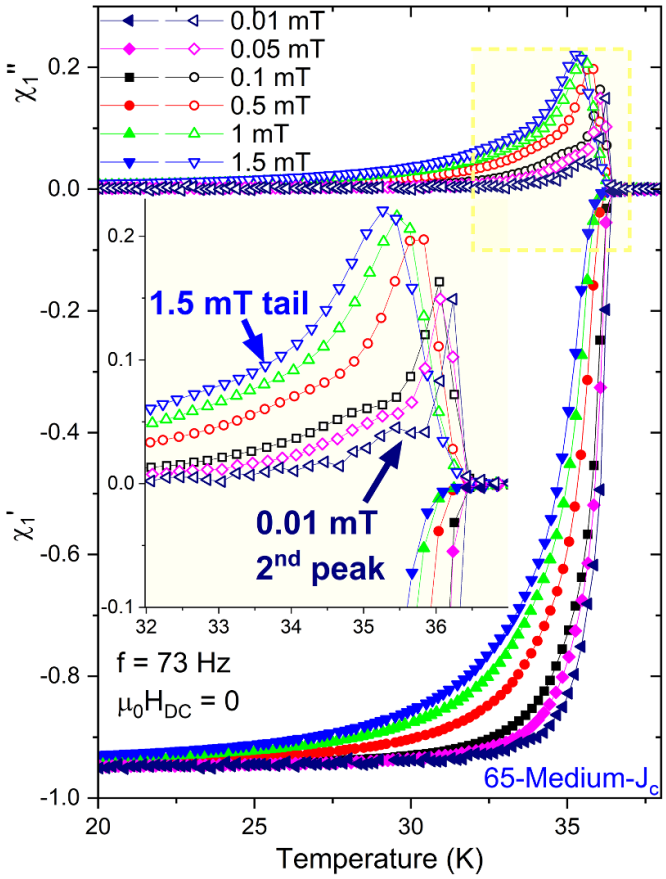

Figure 4. AC susceptibility for the 65-Medium-J_c K-Ba122 sample measured with zero DC field and $\mu_0 H_{ac}$ from 0.01 to 1.5 mT ($f = 73$ Hz). In the inset a magnification of the χ_1'' peaks reveals the appearance of a secondary peak with decreasing H_{ac} amplitude.

To better examine the nature of these transitions, the samples were measured by applying AC field $\mu_0 H_{ac}$ in the 0.01–1.5 mT range (for 100-Higher-J_c, the $\mu_0 H_{ac}$ range was 0.1–1.5 mT). 100-Higher-J_c, shown in figure 3, and 200-Lower-J_c did not exhibit any notable features, showing only the typical narrowing of transitions and peaks as the AC amplitude was decreased. On the other hand, figure 4 shows that, in 65-Medium-J_c sample, the long low-temperature χ_1'' tail gradually develops into a distinct secondary peak as the AC amplitude decreases.

Such a double-peak feature for 65-Medium-J_c is not limited only to the zero DC field data. Figure 5 compares AC susceptibility of this sample up to $\mu_0 H_{DC} = 9$ T with $\mu_0 H_{ac}$ of 1, 0.1 and 0.01 mT, respectively. With $\mu_0 H_{ac} = 1$ mT, there is only one broad feature at all $\mu_0 H_{DC}$ (figure 5(a)), but with decreasing $\mu_0 H_{ac}$ to 0.1 and 0.01 mT, the double χ_1'' peaks and double χ_1' transitions become more apparent as the DC field increases (figures 5(b) and (c)). Notably, at each DC field, the highest-temperature peak and transition of χ_1 are sharper and more pronounced than the lowest-temperature features.

Figure 6 shows a direct comparison of the AC susceptibility at different DC field for the three samples, clearly demonstrating the different nature of the χ_1' transitions and χ_1'' peaks in 65-Medium-J_c compared with the others.

By monitoring the shift of the χ_1'' peak positions as a function of the H_{ac} amplitude and taking into account that J_c is proportional to H_{ac}, we can determine the irreversibility lines (defined by the condition $J_c = 0$) as the limit of the peak position for $H_{ac} \to 0$ [51, 52]. A single irreversibility line can be derived for 100-Higher-J_c and 200-Lower-J_c, which exhibit single χ_1'' peaks. For 65-Medium-J_c sample, where a second peak becomes visible at low H_{ac} amplitude, two irreversibility lines can be determined. The obtained irreversibility lines are shown in figure 7. Both 100-Higher-J_c and 200-Lower-J_c have single irreversibility lines that smoothly increase with decreasing temperature, but they show substantial separation reaching ~4.5 K at 9 T. On the other hand,

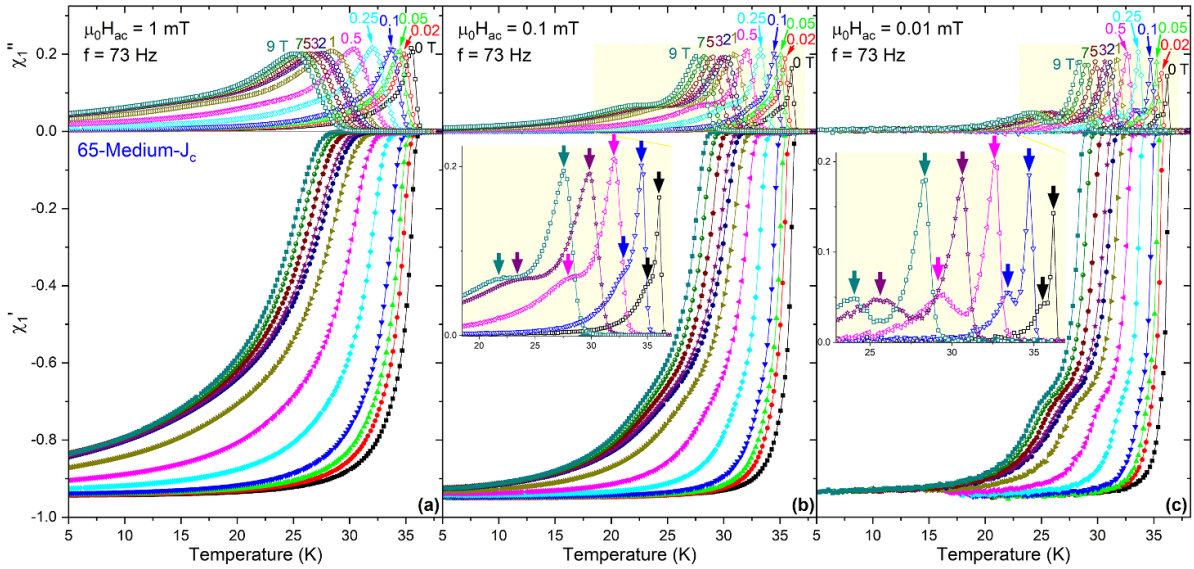

Figure 5. AC susceptibility for the 65-Medium-J_c K-Ba122 sample measured with $\mu_0 H_{DC}$ up to 9 T and with $\mu_0 H_{ac}$ decreasing from (a) 1 mT to (b) 0.1 mT, to (c) 0.01 mT ($f = 73$ Hz). In the insets a magnification of some of the χ_1'' curves reveals the presence of two peaks at the two lowest H_{ac} amplitudes.

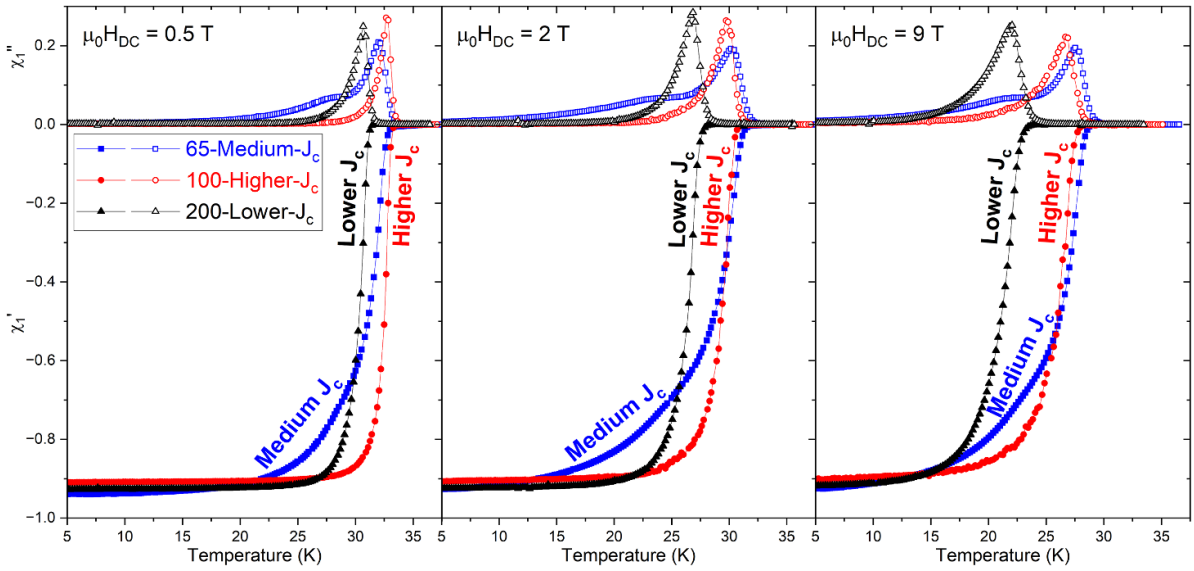

Figure 6. AC susceptibility measured at selected $\mu_0 H_{DC}$ fields of the three K-Ba122 samples showing a marked difference in 65-Medium-J_c ($\mu_0 H_{ac} = 0.1$ mT, f = 73 Hz).

the two lines of 65-Medium-J_c exhibit rather different characteristics. The lower-temperature irreversibility line, which is determined by the small, lower-temperature χ_1'' peak, shows the lowest trace at DC field up to 1–2 T with a strong field dependence, but drastically up-turns above 2 T and becomes the least field dependent irreversibility line (highest slope). The higher-temperature irreversibility line of 65-Medium-J_c, associated with the highest peak, has the best overall trend among all lines in figure 7.

3.3. Microstructural characterization by TEM

S/TEM characterizations also revealed markedly different microstructure of grains and grain boundaries in these K-Ba122 samples. As shown in figure 8, all samples show randomly oriented equiaxed grains with high angle grain boundaries. However, as the milling energy density increases from 65 to 100 and then to 200 MJ kg^{-1}, the average grain size systematically decreases from 128 ± 28 nm to 105 ± 17 nm,

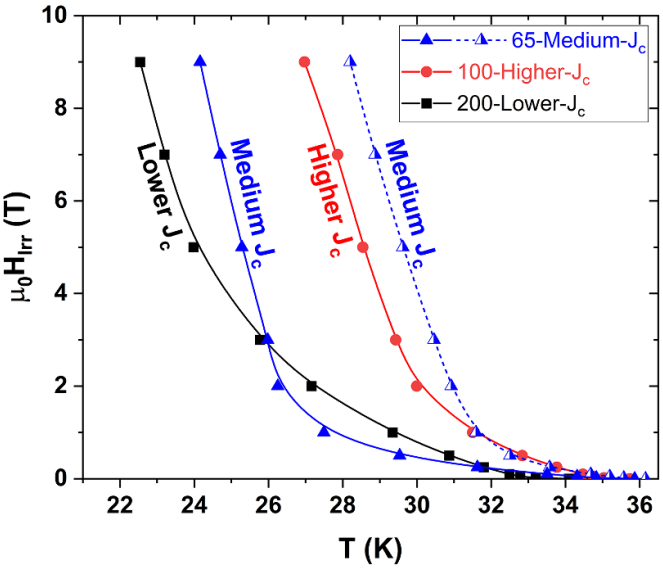

Figure 7. Irreversibility lines determined from the analysis of the AC susceptibility for the three K-Ba122 samples. The double peaks present in 65-Medium-J_c yield two lines (see Discussion). Note that 65-Medium-J_c and 200-Lower-J_c were measured with $\mu_0 H_{ac}$ in the 1.5–0.01 mT range, whereas 100-Higher-J_c was measured from 1.5 to 0.1 mT possibly causing a minor underestimation of its irreversibility line (e.g. underestimated by ∼0.25 K at 9 T).

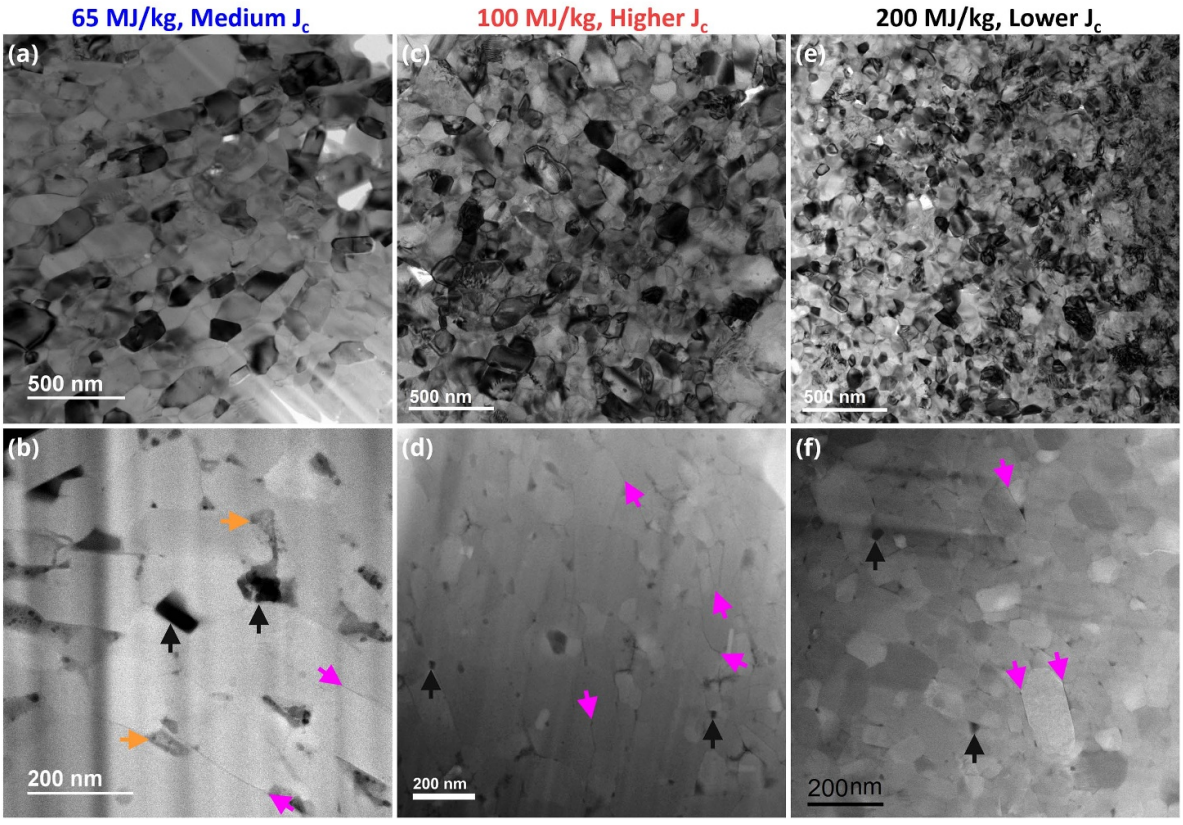

Figure 8. (top) BF- and (bottom) HAADF-STEM microstructures of (a), (b) 65-Medium-J_c, (c), (d) 100-Higher-J_c and (e–f) 200-Lower-J_c samples. The top images reveal a clear reduction of grain size with increasing milling energy. In the bottom images, some of the voids are indicated by vertical black arrows, secondary phase areas by horizontal orange arrows and nano-cracks by magenta arrows tilted in the direction of the crack.

to 70 ± 9 nm, respectively. The sample prepared with the smallest milling energy (65-Medium-J_c in figures 8(a) and (b)) also exhibits many large nano-voids 30–50 nm in size, and secondary phases, mostly Ba-O at the triple junctions of grain boundaries that appear as black or darker contrast in HAADF-STEM (figure 8(b)). In figure 8(b), some GBs show

thin traces of dark HAADF contrast as well. On the other hand, the samples that underwent the intermediate (100-Higher-J_c in figures 8(c) and (d)) and the highest-energy milling (200-Lower-J_c in figures 8(e) and (f)) clearly have lesser amounts of secondary phases at the GB junctions. However, many GB junctions still have small nano-voids 10–30 nm in size, and the dark Z-contrast is also still visible along some GBs. Our recent study of the same samples indicated that such HAADF dark traces along GBs are low-density areas caused by GB nano-cracks, as no composition deviation was detected by TEM-EDS line-scans across GBs [53].

3.4. Sample degradation revealed by AC susceptibility

Following the initial measurements of 100-Higher-J_c (performed prior to 65-Medium-J_c), we decided to perform further AC susceptibility characterizations at lower H_{ac} amplitude on the 100-Higher-J_c sample. In the time lapse between the two runs of measurements, the sample was stored in the high-performance glove box [35], so as to minimize exposing the sample to ambient air, and its surface was mildly polished before the second run to remove possible reaction layer on the surface of the sample. To determine whether the sample properties were unchanged, we first measured it in the same conditions as the first run but, as shown in figure 9, we found notable differences in AC susceptibility between the two runs. In fact, the two AC susceptibility measurements ($\mu_0 H_{ac} = 0.1$ mT and no DC field) reveal that the originally sharp transition and peak transformed into a rather broad χ_1' transition and a double χ_1'' peak with an extended low-temperature tail. Despite these changes, the position of the highest-temperature χ_1'' peak remains unaltered.

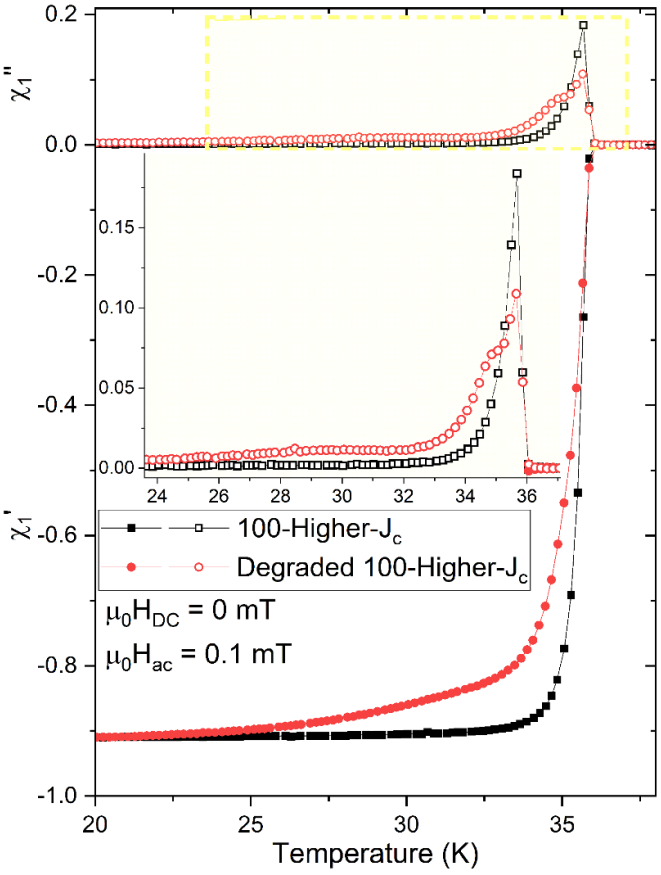

Figure 9. AC susceptibility measured with zero DC field and $\mu_0 H_{ac} = 0.1$ mT ($f = 73$ Hz) of the original 100 MJ kg^{-1} sample (black data) and of the same sample after degradation (red data) showing in the latter a significant broadening of the χ_1' transition and the appearance of a double χ_1'' peak with a long low-temperature tail.

4. Discussion

The different field dependences of the magnetization J_c (figure 1) gives us some insights about the differences in superconducting properties between samples. Despite their notable J_c difference, 100-Higher-J_c and 200-Lower-J_c have similar low-field J_c trends. On the other hand, the sharp decline at low field for 65-Medium-J_c is typically recognized as a sign of GB weak-links. The double cross-over with 200-Lower-J_c at 0.5–1 T emphasized the sharp change in field dependence. In fact, in the case of 65-Medium-J_c, the field dependence is the strongest at low-field but the weakest at high field when compared to the other two samples. Also, at higher fields, 200-Lower-J_c clearly exhibits the weakest in-field J_c performance compared to the other two samples.

As previously mentioned, AC susceptibility is generally useful to evaluate sample granularity. However, our present results suggest a quite different scenario. Unlike typical granular materials that exhibit a clear separation between intra- and INTER-grain contributions [38–45], in our K-Ba122 samples the features associated with the intra-grain component are rather small (figure 2 and table 2) and do not show a correspondent intra-grain χ_1'' peak. These features reveal limited sample-to-sample difference in the $T_{c,intra}$ onset (37.2–38.0 K) whose value is compatible with single crystals and large-grain polycrystalline samples [3, 36, 54, 55]. However, the small intra-grain signal is not necessarily a sign of good connectivity, because the grain size in all these samples is smaller than the penetration depth, making detection of the intra-grain signal very hard [48]. In contrast, the onset of the sharp INTER-grain diamagnetic signal reveals clear sample-to-sample variation (34.5–36.5 K) with 200-Lower-J_c showing notably inferior performance. Interestingly, the best INTER- and intra-grain T_c onsets are measured in 65-Medium-J_c but they are not sufficient to generate high J_c because of the broad INTER-grain T_c transition.

The secondary χ_1'' peak in 65-Medium-J_c, which appears as the AC field decreases, raises the question of whether those features (and not those described in the previous paragraph) could be ascribed to the intra-/INTER-grain contributions. However, as mentioned earlier, previous studies showed that,

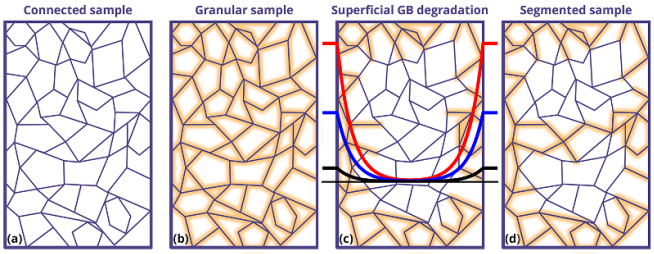

Figure 10. Schematics of possible scenarios for polycrystalline samples: (a) Connected sample, with clean and connected GBs; (b) Granular sample, with compromised GBs resulting into disconnected grains (represented by orange areas); (c) Superficial GB degradation, where the compromised GBs are present near the sample surface; (d) Subdivided sample, where the compromised GBs could also involve GBs across the sample subdividing it into several macroscopic areas, which are well-connected in their centers. In (c) the red, blue, and black thick lines represent the field penetration in the sample with decreasing field amplitude.

in granular polycrystalline $YBa_2Cu_3O_x$ and $FeSe_{0.5}Te_{0.5}$ [38, 45, 46], the lower-temperature INTER-grain peak is typically the most prominent and its amplitude is largely unaffected by H_{ac}. In our sample, the predominant χ_1'' peak is at the highest temperature indicating that it has to be associated with the INTER-grain contribution.

To better understand what causes the secondary low-temperature χ_1'' peak, we need to consider different scenarios related to the nature of the superconducting sample. Figure 10 schematically illustrates a few examples: (a) a fully connected sample with GBs that do not block current with a single INTER-grain peak, (b) a granular sample whose GBs are fully compromised and block current (current-blocking GBs are marked by orange highlights), which would generate a single INTER-grain peak (and, if detectable, a small intra-grain peak at higher temperature), (c) a scenario where compromised GBs are more prevalent near the sample surface, leaving the center of the sample well-connected, which would lead to two INTER-grain peaks determined by different levels of connectivity and (d) a scenario where compromised GBs subdivide the sample into macroscopic but separated areas that are still internally well-connected, leading again to two INTER-grain peaks (one due to the entire sample and one due to sub-divided parts). The secondary χ_1'' peak emerging at low H_{ac} amplitude (figure 4) is most likely associated to the third (c) or the fourth (d) scenario with two INTER-grain contributions. In fact, the field penetration represented in figure 10(c) shows that with a large H_{ac} amplitude the well-connected sample interior is exposed to large field producing a dominant signal. Differently, with decreasing H_{ac}, the amplitude of the field on the sample interior is smaller producing a smaller signal, substantially making the measurement more sensitive to the properties of the sample surface and allowing the detection of the weaker surface signal. When this superficial region has obviously different properties with respect to the sample interior, χ_1'' reveals separate features. The fourth scenario (d) could produce a similar two-contribution feature because of the easy field penetration into the regions subdividing the sample, which would behave similarly to the sample surface as described in scenario (c). Applying high DC field, these features become even more separated (figure 5) leading to the two irreversibility lines for the 65-Medium-J_c sample. The importance of these two lines needs further discussion.

Figure 7 shows that 100-Higher-J_c appears well-connected, but its irreversibility line is not optimal. 200-Lower-J_c sample appears reasonably connected as well but its irreversibility line shows a rather strong field-dependence, suggesting that the extended milling might be detrimental for the K-Ba122 properties. On the other hand, the 65-Medium-J_c has some connectivity and/or homogeneity issues. Its lower-temperature line (solid blue triangles in figure 7) has a sharp up-turn between 1 and 2 T, a feature frequently associated with weak-link behavior. However, at low temperature and high DC field, this irreversibility line falls between the lines of the 200-Lower-J_c and the 100-Higher-J_c samples, suggesting that it is indeed this line that determines the overall low-temperature J_c performance of 65-Medium-J_c (see figure 1). The higher-temperature irreversibility line of 65-Medium-J_c (half blue triangles in figure 7) is, on the other hand, the highest-temperature curve, implying that there is a part of the sample with much better properties than those determining the lower-temperature irreversibility line, and also better than in 100-Higher-J_c. This better part of the sample has to be much larger than the grains but smaller than the entire bulk sample. This high-temperature irreversibility line also implies that, in general, better performance in K-Ba122 bulk samples is achievable if we can identify what prevents their development on a macroscopic scale.

The hypothesis that the secondary peak originates from either superficial compromised GBs or the macroscopic subdivision of sample seems to be consistent with the unexpected property changes of 100-Higher-J_c when remeasured (figure 9). In fact, the sample clearly suffered from some kind of degradation, resulting in AC susceptibility features similar to those in the pristine 65-Medium-J_c sample.

The possible cause of the sample-to-sample differences can be found in their microstructures (figure 8). With increasing milling energy, the nano-voids progressively decrease in number and size, resulting in an increase of sample density. This microstructural difference is plausibly related to the particle sizes in the powder before the second HT: for 65-Medium-J_c, the low milling energy leaves larger particles preventing an effective HIP densification. This large-void microstructure likely facilitates the sample subdivision or possibly, since the void network most likely reaches the sample surface, could make this sample more susceptible to degradation with short exposure. The observed decrease of secondary phases with increasing E_{BM} above 65 MJ kg^{-1} is likely due to improved powder mixing, which results in a more homogeneous and more complete reaction into the main K-Ba122 phase preventing the formation of large quantities of secondary phases. 100-Higher-J_c originally had very sharp transitions making it the most homogeneous and the most well-connected. The appearance of the secondary features when 100-Higher-J_c was

remeasured could be caused by some degradation occurring because of increased exposure to air, but it could also be due to the additional thermal stress during the second cooling down to cryogenic temperature causing the nano-cracks to expand. In fact, in some cases, we did notice samples being hard solids when installed in the PPMS but partially fractured when taken out after being measured. Since nano-cracks do not cause compositional variation, the increased density of cracks can hardly be observed by conventional microscopes, thus new techniques will have to be developed [56]. A possible thin reaction layer due to exposure, which could cause local variation of composition, would require the resolution that only atom probe tomography can provide, but only on sophisticated specimens made of few grains.

These nano-cracks at GBs are clearly detrimental for the overall performance because they reduce the sample effective cross-section. We will have to identify the origin of their formations and find a strategy to prevent them. We presently suspect two possible causes: the large stress the samples undergo when the pressure and temperature are reduced in the HIP, or when the crucible is cut and opened to extract the K-Ba122 phase. In the first case, a more controlled and gradual temperature reduction and pressure release could be beneficial. The second case would probably require producing samples that would not need to be removed from the external metal container, either by making wires with a hard sheath [20] or by making large bulk samples with reinforcing rings [57].

Regarding the synthesis process, certainly of interest would be further optimization, including investigation of the performance of samples prepared with a wider range of milling energy densities or by varying other synthesis parameters. But the primary goal of this paper is to highlight the connectivity issues in polycrystalline K-Ba122 that can be difficult to detect by standard characterizations, but can be detected analyzing AC susceptibility measurements, a technique that is currently underutilized but has the great potential to reveal hidden features such as connectivity.

5. Conclusions

In this work we systematically investigated the temperature and field dependence of the AC susceptibility of three small-grain-size polycrystalline K-doped Ba122 samples prepared by varying the milling energy density (65–200 MJ kg^{-1}) in the first stage of a two-stage preparation and synthesis process and maintaining all other parameters unaltered. The resulting samples had obviously different critical current performance, with the best J_c achieved at the intermediate milling (100 MJ kg^{-1}), and different microstructures. In fact, the microstructures go from a porous sample with large nano-voids and secondary phases (possibly caused by limited mixing) at 65 MJ kg^{-1}, to samples with a few small nano-voids but with visible nano-cracks at grain boundaries at 100–200 MJ kg^{-1}. We also observed that the grain size progressively decreased with increasing milling energy.

The AC susceptibility analysis was able to identify a relatively high intra-grain T_c onset, compatible with single crystals and large-grain polycrystalline samples but generating a barely detectable diamagnetic signal. The main diamagnetic INTER-grain onset is instead found at lower temperature (34.5–36.5 K). Both intra- and INTER-grain onsets systematically decrease with increasing milling energy density, possibly because of the decreasing grain size. Apart from the T_c difference, we noticed a much broader χ_1' transition and χ_1'' peak for the 65 MJ kg^{-1} sample. To compare the irreversibility lines of our samples we investigated the H_{ac} amplitude dependence in DC field up to 9 T. Differently from the other samples, this revealed markedly different properties in the 65 MJ kg^{-1} case with the appearance of secondary peaks on the low-temperature side of the χ_1'' peak and with the development of a double χ_1' transition. This was associated with the presence of compromised GBs near the sample surface leaving the center well-connected or to compromised GBs that subdivide the sample into macroscopic areas still well-connected in their centers. Because of the χ_1'' peak splitting, two irreversibility lines were determined for the 65 MJ kg^{-1} sample, whereas only one each was determined for the 100 and 200 MJ kg^{-1} samples. Interestingly, the comparison between the irreversibility lines and J_c suggested that it is the worst 65 MJ kg^{-1} irreversibility line that determines its J_c performance, making the sample subdivision the most likely scenario. It is important to notice that the best J_c-performing sample (100 MJ kg^{-1}) has an irreversibility line slightly inferior to the highest-temperature line of the 65 MJ kg^{-1} sample, associated with the well-connected portion of this sample. This implies that further improvement of performance can be achieved.

Data availability statement

The data that support the findings of this study are openly available at the following URL/DOI: https://osf.io/ctnzg/ [58].

Acknowledgment

This work was supported by the US Department of Energy Office of High Energy Physics under the Grant Numbers DE-SC0018750, and it was performed at the National High Magnetic Field Laboratory, which is supported by National Science Foundation Cooperative Agreements NSF DMR-2128556, and by the State of Florida.

ORCID iDs

Chiara Tarantini https://orcid.org/0000-0002-3314-5906
Eric E Hellstrom https://orcid.org/0000-0001-8263-8662
Fumitake Kametani https://orcid.org/0000-0002-1067-9331

References

[1] Kamihara Y, Hiramatsu H, Hirano M, Kawamura R, Yanagi H, Kamiya T and Hosono H 2006 Iron-based layered superconductor: LaOFeP *J. Am. Chem. Soc.* **128** 10012–3

[2] Kamihara Y, Watanabe T, Hirano M and Hosono H 2008 Iron-based layered superconductor La[$O_{1-x}F_x$]FeAs (x = 0.05−0.12) with T_c = 26 K *J. Am. Chem. Soc.* **130** 3296–7

[3] Rotter M, Tegel M and Johrendt D 2008 Superconductivity at 38 K in the iron arsenide ($Ba_{1-x}K_x$) Fe_2As_2 *Phys. Rev. Lett.* **101** 107006

[4] Hsu F-C *et al* 2008 Superconductivity in the PbO-type structure α-FeSe *PNAS* **105** 14262–4

[5] Iyo A, Kawashima K, Kinjo T, Nishio T, Ishida S, Fujihisa H, Gotoh Y, Kihou K, Eisaki H and Yoshida Y 2016 New-structure-type Fe-based superconductors: $CaAFe_4As_4$ (A = K, Rb, Cs) and $SrAFe_4As_4$ (A = Rb, Cs) *J. Am. Chem. Soc.* **138** 3410–5

[6] Hosono H, Yamamoto A, Hiramatsu H and Ma Y 2018 Recent advances in iron-based superconductors toward applications *Mater. Today* **21** 278–302

[7] Ren Z-A, Lu W, Yang J, Yi W and Shen X-L 2008 Superconductivity at 55 K in iron-based F-doped layered quaternary compound Sm[$O_{1-x}F_x$]FeAs *Chin. Phys. Lett.* **25** 2215

[8] Hunte F, Jaroszynski J, Gurevich A, Larbalestier D C, Jin R, Sefat A S, McGuire M A, Sales B C, Christen D K and Mandrus D 2008 Two-band superconductivity in $LaFeAsO_{0.89}F_{0.11}$ at very high magnetic fields *Nature* **453** 903–5

[9] Baily S A, Kohama Y, Hiramatsu H, Maiorov B, Balakirev F F, Hirano M and Hosono H 2009 Pseudoisotropic upper critical field in cobalt-doped $SrFe_2As_2$ epitaxial films *Phys. Rev. Lett.* **102** 117004

[10] Tarantini C, Gurevich A, Jaroszynski J, Balakirev F, Bellingeri E, Pallecchi I, Ferdeghini C, Shen B, Wen H H and Larbalestier D C 2011 Significant enhancement of upper critical fields by doping and strain in iron-based superconductors *Phys. Rev.* B **84** 184522

[11] Hanzawa K, Matsumoto J, Iimura S, Kohama Y, Hiramatsu H and Hosono H 2022 High upper critical field (120 T) with small anisotropy of highly hydrogen-substituted SmFeAsO epitaxial film *Phys. Rev. Mater.* **6** L111801

[12] Sefat A S, Jin R, McGuire M A, Sales B C, Singh D J and Mandrus D 2008 Superconductivity at 22 K in co-doped $BaFe_2As_2$ crystals *Phys. Rev. Lett.* **101** 117004

[13] Jiang S, Xing H, Xuan G, Wang C, Ren Z, Feng C, Dai J, Xu Z and Cao G 2009 Superconductivity up to 30 K in the vicinity of the quantum critical point in $BaFe_2(As_{1-x}P_x)_2$ *J. Phys.: Condens. Matter* **21** 382203

[14] Altarawneh M M, Collar K, Mielke C H, Ni N, Bud'ko S L and Canfield P C 2008 Determination of anisotropic H_{c2} up to 60 T in $Ba_{0.55}K_{0.45}Fe_2As_2$ single crystals *Phys. Rev.* B **78** 220505

[15] Yamamoto A *et al* 2009 Small anisotropy, weak thermal fluctuations, and high field superconductivity in Co-doped iron pnictide $Ba(Fe_{1-x}Co_x)_2As_2$ *Appl. Phys. Lett.* **94** 062511

[16] Hatano T, Qin D, Iida K, Gao H, Guo Z, Saito H, Hata S, Shimada Y, Naito M and Yamamoto A 2024 High tolerance of the superconducting current to large grain boundary angles in potassium-doped $BaFe_2As_2$ *NPG Asia Mater.* **16** 41

[17] Dong C, Xu Q and Ma Y 2024 Towards high-field applications: high-performance, low-cost iron-based superconductors *Natl Sci. Rev.* **11** nwae122

[18] Weiss J D, Tarantini C, Jiang J, Kametani F, Polyanskii A A, Larbalestier D C and Hellstrom E E 2012 High intergrain critical current density in fine-grain ($Ba_{0.6}K_{0.4}$)Fe_2As_2 wires and bulks *Nat. Mater.* **11** 682–5

[19] Pyon S, Suwa T, Tamegai T, Takano K, Kajitani H, Koizumi N, Awaji S, Zhou N and Shi Z 2018 Improvements of fabrication processes and enhancement of critical current densities in (Ba,K)Fe_2As_2 HIP wires and tapes *Supercond. Sci. Technol.* **31** 055016

[20] Gao Z, Togano K, Zhang Y, Matsumoto A, Kikuchi A and Kumakura H 2017 High transport J_c in stainless steel/Ag-Sn double sheathed Ba122 tapes *Supercond. Sci. Technol.* **30** 095012

[21] Pyon S, Ito T, Sakagami R, Tamegai T, Awaji S, Kito H, Ishida S, Eisaki H, Yoshida Y and Kajitani H 2023 Fabrication of multi-filament(Ba,A)Fe_2As_2 (A: Na, K) HIP round wires and a small superconducting coil *Supercond. Sci. Technol.* **36** 015009

[22] Gao Z, Togano K, Matsumoto A and Kumakura H 2014 Achievement of practical level critical current densities in $Ba_{1-x}K_xFe_2As_2$/Ag tapes by conventional cold mechanical deformation *Sci. Rep.* **4** 4065

[23] Guo Z, Gao H, Kondo K, Hatano T, Iida K, Hänisch J, Ikuta H and Hata S 2021 Nanoscale texture and microstructure in a NdFeAs(O,F)/IBAD-MgO superconducting thin film with superior critical current properties *ACS Appl. Electron. Mater.* **3** 3158–66

[24] Iida K, Sato H, Tarantini C, Hänisch J, Jaroszynski J, Hiramatsu H, Holzapfel B and Hosono H 2017 High-field transport properties of a P-doped $BaFe_2As_2$ film on technical substrate *Sci. Rep.* **7** 39951

[25] Liu L *et al* 2023 Fabrication of meter-long class Fe(Se,Te)-coated conductors with high superconducting performance *Adv. Eng. Mater.* **25** 2201536

[26] Iida K *et al* 2011 Epitaxial growth of superconducting $Ba(Fe_{1-x}Co_x)_2As_2$ thin films on technical ion beam assisted deposition MgO substrates *Appl. Phys. Express* **4** 013103

[27] Piperno L *et al* 2024 Low-cost architecture for iron-based coated conductors *iScience* **27** 111032

[28] Fang L *et al* 2012 High, magnetic field independent critical currents in (Ba,K)Fe_2As_2 crystals *Appl. Phys. Lett.* **101** 012601

[29] Ishida S, Song D, Ogino H, Iyo A, Eisaki H, Nakajima M, Shimoyama J and Eisterer M 2017 Doping-dependent critical current properties in K, Co, and P-doped $BaFe_2As_2$ single crystals *Phys. Rev.* B **95** 014517

[30] Mishev V, Nakajima M, Eisaki H and Eisterer M 2016 Effects of introducing isotropic artificial defects on the superconducting properties of differently doped Ba-122 based single crystals *Sci. Rep.* **6** 27783

[31] Qin D, Iida K, Hatano T, Saito H, Ma Y, Wang C, Hata S, Naito M and Yamamoto A 2021 Realization of epitaxial thin films of the superconductor K-doped $BaFe_2As_2$ *Phys. Rev. Mater.* **5** 014801

[32] Iida K *et al* 2021 Approaching the ultimate superconducting properties of (Ba,K)Fe_2As_2 by naturally formed low-angle grain boundary networks *NPG Asia Mater.* **13** 68

[33] Cheng Z, Dong C, Yang H, Zhang Q, Awaji S, Gu L, Wen H-H and Ma Y 2022 Strengthened proximity effect at grain boundaries to enhance inter-grain supercurrent in $Ba_{1-x}K_xFe_2As_2$ superconductors *Mater. Today Phys.* **28** 100848

[34] Kametani F, Su Y-F, Tarantini C, Hellstrom E E, Matsumoto A, Kumakura H, Togano K, Huang H and Ma Y 2023 On the mechanisms of J_c increment and degradation in high J_c Ba122 tapes made by the different processing *Appl. Phys. Express* **17** 013004

[35] Pak C, Su Y F, Collantes Y, Tarantini C, Hellstrom E E, Larbalestier D C and Kametani F 2020 Synthesis routes to

eliminate oxide impurity segregation and their influence on intergrain connectivity in K-doped $BaFe_2As_2$ polycrystalline bulks *Supercond. Sci. Technol.* **33** 084010

[36] Tokuta S, Hasegawa Y, Shimada Y and Yamamoto A 2022 Enhanced critical current density in K-doped Ba122 polycrystalline bulk superconductors via fast densification *iScience* **25** 103992

[37] Tokuta S, Shimada Y and Yamamoto A 2020 Evolution of intergranular microstructure and critical current properties of polycrystalline Co-doped $BaFe_2As_2$ through high-energy milling *Supercond. Sci. Technol.* **33** 094010

[38] Goldfarb R B, Clark A F, Braginski A I and Panson A J 1987 Evidence for two superconducting components in oxygen-annealed single-phase Y–Ba–Cu–O *Cryogenics* **27** 475–80

[39] Goldfarb R B, Lelentan M and Thompson C A 1991 *Alternating-field Susceptometry and Magnetic Susceptibility of Superconductors Magnetic Susceptibility of Superconductors and Other Spin Systems* ed T L Francavilla, R A Hein and D H Liebenberg (Plenum Press) p 49

[40] Nikolo M and Goldfarb R B 1989 Flux creep and activation energies at the grain boundaries of Y-Ba-Cu-O superconductors *Phys. Rev.* B **39** 6615–8

[41] Chen D-X, Nogues J and Rao K V 1989 A.c. susceptibility and intergranular critical current density of high T_c superconductors *Cryogenics* **29** 800–8

[42] Forsthuber M, Ludwig F and Hilscher G 1991 Size dependence of the AC susceptibility and critical current densities of ceramic high-T_c superconductors *Physica* C **177** 401–14

[43] Rani P, Hafiz A K and Awana V P S 2016 Improvement in granularity of $NdFeAsO_{0.8}F_{0.2}$ superconductor through Ag_x doping (x = 0.0–0.3) *Physica* C **520** 1–7

[44] Aswathy P M, Anooja J B, Syamaprasad U and Clarke D 2013 $NdFeAsO_{1-x}F_x$ superconductor—impact of fluorine variation on microstructure and transport properties *J. Am. Ceram. Soc.* **96** 1176–80

[45] Mancusi D, Polichetti M, Cimberle M R and Pace S 2015 Influence of the interaction between the inter- and intragranular magnetic responses in the analysis of the ac susceptibility of a granular $FeSe_{0.5}Te_{0.5}$ superconductor *Supercond. Sci. Technol.* **28** 095017

[46] Nikolo M 1995 Superconductivity: a guide to alternating current susceptibility measurements and alternating current susceptometer design *Am. J. Phys.* **63** 57–65

[47] Häßler W, Hermann H, Herrmann M, Rodig C, Aubele A, Schmolinga L, Sailer B and Holzapfel B 2013 Influence of the milling energy transferred to the precursor powder on the microstructure and the superconducting properties of MgB_2 wires *Supercond. Sci. Technol.* **26** 025005

[48] Tarantini C, Pak C, Su Y-F, Hellstrom E E, Larbalestier D C and Kametani F 2021 Effect of heat treatments on superconducting properties and connectivity in K-doped $BaFe_2As_2$ *Sci. Rep.* **11** 3143

[49] Limon S A 2024 Effects of synthesis parameters on superconducting properties of polycrystalline K-doped Ba-122 *PhD Thesis* The Florida State University

[50] Prozorov R and Kogan V G 2018 Effective demagnetizing factors of diamagnetic samples of various shapes *Phys. Rev. Appl.* **10** 014030

[51] Dhingra I and Das B K 1993 Frequency, field and thermomagnetic dependence of AC susceptibility in YBCO *Supercond. Sci. Technol.* **6** 765–70

[52] van Huong C N, Nicolas M, Negri J and Burger J P 1991 Diamagnetism and irreversibility lines in $EuBa_{2-x}K_xCu_3O_7$ compounds *Supercond. Sci. Technol.* **4** 711–6

[53] Kametani F, Limon S A, Mao K, Hellstrom E and Tarantini C 2025 Remnant magnetization behavior of a K-doped Ba122 polycrystalline bulk *IEEE Trans. Appl. Supercond.* **35** 7300205

[54] Liu Y, Tanatar M A, Straszheim W E, Jensen B, Dennis K W, McCallum R W, Kogan V G, Prozorov R and Lograsso T A 2014 Comprehensive scenario for single-crystal growth and doping dependence of resistivity and anisotropic upper critical fields in $(Ba_{1-x}K_x)Fe_2As_2$ ($0.22 \leqslant x \leqslant 1$) *Phys. Rev.* B **89** 134504

[55] Nakajima M *et al* 2014 Normal-state charge dynamics in doped $BaFe_2As_2$: roles of doping and necessary ingredients for superconductivity *Sci. Rep.* **4** 5873

[56] Kametani F, Limon S A, Jani M R, Su Y-F, Mao K, Tarantini C and Hellstrom E E 2024 On the mechanisms of Jc increment and degradation in K-doped Ba122 polycrystalline bulks, wires and tapes. *Applied Superconductivity Conf.*

[57] Durrell J H *et al* 2014 A trapped field of 17.6 T in melt-processed, bulk Gd-Ba-Cu-O reinforced with shrink-fit steel *Supercond. Sci. Technol.* **27** 082001

[58] Tarantini C 2025 AC characterization of bulk K-doped Ba122 *OSF repository* (available at: https://osf.io/ctnzg/)